

Dense magnetized plasma associated with a fast radio burst

Kiyoshi Masui^{1,2}, Hsiu-Hsien Lin³, Jonathan Sievers^{4,5}, Christopher J. Anderson⁶, Tzu-Ching Chang⁷, Xuelei Chen^{8,9}, Apratim Ganguly¹⁰, Miranda Jarvis¹¹, Cheng-Yu Kuo^{12,7}, Yi-Chao Li⁸, Yu-Wei Liao⁷, Maura McLaughlin¹³, Ue-Li Pen^{14,2,15}, Jeffrey B. Peterson³, Alexander Roman³, Peter T. Timbie⁶, Tabitha Voytek^{4,3} & Jaswant K. Yadav¹⁶

Fast Radio Bursts are bright, unresolved, non-repeating, broadband, millisecond flashes, found primarily at high Galactic latitudes, with dispersion measures much larger than expected for a Galactic source¹⁻⁸. The inferred all-sky burst rate⁹ is comparable to the core-collapse supernova rate¹⁰ out to redshift 0.5. If the observed dispersion measures are assumed to be dominated by the intergalactic medium, the sources are at cosmological distances with redshifts^{11,12} of 0.2 to 1. These parameters are consistent with a wide range of source models¹³⁻¹⁸. One fast radio burst⁶ showed circular polarization [21(7)%] of the radio emission, but no linear polarization was detected, and hence no Faraday rotation measure could be determined. Here we report the examination of archival data revealing Faraday rotation in a newly detected burst—FRB 110523. It has radio flux at least 0.6 Jy and dispersion measure 623.30(5) pc cm⁻³. Using Galactic contribution 45 pc cm⁻³ and a model of intergalactic electron density¹¹, we place the source at a maximum redshift of 0.5. The burst has rotation measure -186.1(1.4) rad m⁻², much higher than expected for this line of sight through the Milky Way and the intergalactic medium, indicating magnetization in the vicinity of the source itself or within a host galaxy. The pulse was scattered by two distinct plasma screens during propagation, which requires either a dense nebula associated with the source or a location within the central region of its host galaxy. Keeping in mind that there may be more than one type of fast radio burst source, the detection in this instance of source-local magnetization and scattering favours models involving young stellar populations such as magnetars over models involving the mergers of older neutron stars, which are more likely to be located in low density regions of the host galaxy.

We searched for FRBs in a data archive we collected for the Green Bank Hydrogen Intensity Mapping survey¹⁹⁻²¹. The data span the frequency range 700 to 900 MHz in 4096 spectral channels. Average spectra are recorded at 1.024 ms intervals. We developed a new tree dedispersion algorithm and associated computer program to search for FRBs. First we

removed cold plasma dispersion, a frequency-dependent time delay

$$t_{\text{delay}} = 4148.808 \text{ s} \left(\frac{\text{DM}}{\text{pc cm}^{-3}} \right) \left(\frac{\text{MHz}^2}{\nu^2} \right),$$

where ν is the radio frequency and the dispersion measure, $\text{DM} = \int n_e dl$, is the line of sight integral of the free electron number density. We then summed all frequency channels for DM values ranging from 0 to 2000 pc cm⁻³ and flagged as candidates all data sets with eight- σ positive excursions of flux. These 6496 candidates were examined by eye and compared to synthetic DM-time images of simulated FRB events. Most of these candidates have the characteristics of radio frequency interference (RFI) but one matched the expected pattern of an FRB (see Figure 1 and Extended Data Figure 1). This burst, hereafter FRB 110523, has a DM of 623.30(6) pc cm⁻³; the maximum DM expected in this direction due to Galactic contributions²² is 45 pc cm⁻³. Detailed parameters for the burst are given in Extended Data Table 1.

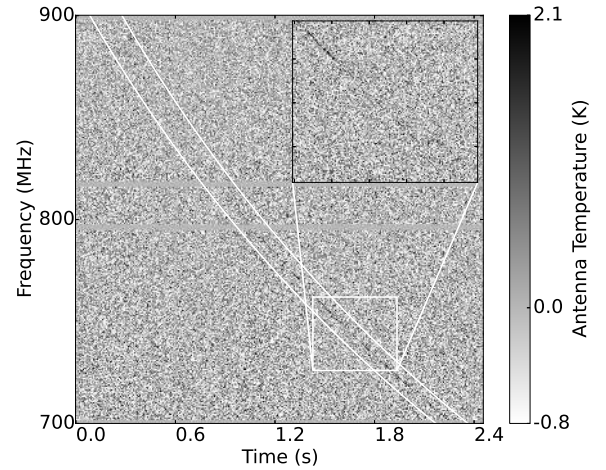


Figure 1: Brightness temperature spectra vs time for FRB 110523. The diagonal curve shows the pulse of radio brightness sweeping in time. The arrival time is differentially delayed (dispersed) by plasma along the line of sight. A pair of curves in white have been added, bracketing the FRB pulse, to show that the delay function matches that expected from cold plasma. The gray horizontal bars show where data has been omitted due to resonances within the GBT receiver. The inset shows fluctuations in brightness caused by scintillation.

Our detection in a distinct band and with independent instrumentation compared to the 1.4 GHz detections at the Parkes and Arecibo observatories greatly strengthens the case that FRBs are astrophysical phenomena. In addition, as described in the Methods, the close fits to astronomical expectations for dispersion spectral index, Faraday rotation, and scattering spectral index all further support an astronomical origin.

Fitting a model to the burst data we find the detection significance is over 40σ , with fluence 3.79(15) K ms at our centre spectral frequency of 800 MHz. The burst has a steep spectral index -7.8(4) which we attribute to telescope motion. The peak antenna temperature at 800 MHz is 1.16(5) K. We do not know the location of the source within the GBT beam profile, but if the source location were at beam centre where the antenna gain is 2 K Jy⁻¹ the measured antenna temperature would translate to 0.6 Jy. Off

¹Department of Physics and Astronomy, University of British Columbia, 6224 Agricultural Rd, Vancouver, BC, V6T 1Z1, Canada

²Canadian Institute for Advanced Research, CIFAR Program in Cosmology and Gravity, Toronto, ON, M5G 1Z8

³McWilliams Center for Cosmology, Carnegie Mellon University, Department of Physics, 5000 Forbes Ave, Pittsburgh, PA, 15213, USA

⁴Astrophysics and Cosmology Research Unit, School of Chemistry and Physics, University of KwaZulu-Natal, Durban, 4001, South Africa

⁵National Institute for Theoretical Physics (NITheP), KZN node, Durban, 4001, South Africa

⁶Department of Physics, University of Wisconsin, Madison, WI 53706-1390, USA

⁷Academia Sinica Institute of Astronomy and Astrophysics, 11F of Astro-Math Building, AS/NTU, 1, Sec. 4, Roosevelt Rd, Taipei 10617, Taiwan

⁸National Astronomical Observatories, Chinese Academy of Science, 20A Datun Road, Beijing 100012, China

⁹Center of High Energy Physics, Peking University, Beijing 100871, China

¹⁰Astrophysics and Cosmology Research Unit, School of Mathematics, Statistics, and Computer Science, University of KwaZulu-Natal, Durban, 4001, South Africa

¹¹Department of Astronomy & Astrophysics, University of Toronto, 50 St George St, Toronto, ON, M5S 3H4, Canada

¹²Department of Physics, National Sun Yat-Sen University No.70, Lianhai Rd., Gushan Dist., Kaohsiung City 804, Taiwan

¹³Department of Physics and Astronomy, West Virginia University, Morgantown WV 26506, USA

¹⁴Canadian Institute for Theoretical Astrophysics, 60 St George St, Toronto, ON, M5S 3H8, Canada

¹⁵Perimeter Institute, 31 Caroline St, Waterloo, Canada

¹⁶Indian Institute of Science Education and Research Mohali, Knowledge City, Sector 81, SAS Nagar, Manauli PO 140306, India

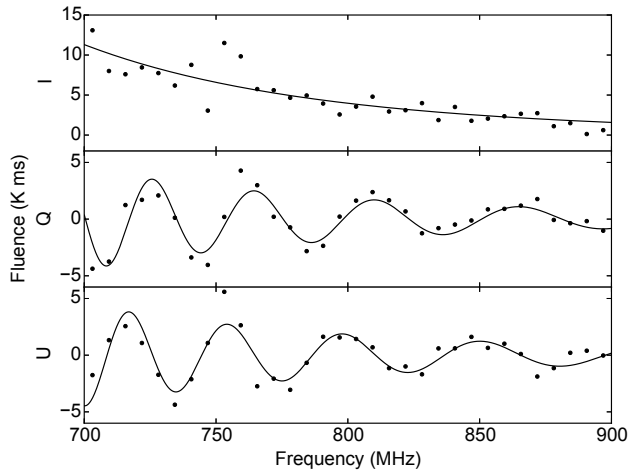


Figure 2: **FRB 110523 spectra in total intensity and polarization.** Plotted is the pulse energy for total intensity (Stokes I), and linear polarization (Stokes Q, and U). Solid curves are model fits. In addition to noise, scatter in the measurement around the models is due to the scintillation visible in Figure 1. The decline of intensity with frequency is primarily due to motion of the telescope beam across the sky and is not intrinsic to the source.

centre the antenna has lower gain so this is a lower limit to the FRB flux, similar to that of previously reported FRBs. The intrinsic FWHM duration of the burst (with scattering removed) is 1.74(17) ms, also similar to the widths of previously reported FRBs.

Allowing the dispersion relation to vary in the model, we find that the dispersive delay is proportional to $t_{\text{delay}} \sim \nu^{-1.998(3)}$, in close agreement to the expected ν^{-2} dependence for a cold, diffuse plasma. Following Katz²³, this provides an upper limit on the density of electrons in the dispersing plasma of $n_e < 1.3 \times 10^7 \text{ cm}^{-3}$ at 95% confidence and a lower limit on the size of the dispersive region of $d > 10 \text{ AU}$. This limit improves upon limits from previous bursts^{23–25} and rules out a flare star as the source of FRB 110523, as stellar corona are denser and less extended by at least an order of magnitude²⁶. Flare stars being the last viable Galactic-origin model for FRB sources, we take the source to be extragalactic.

We find strong linear polarization, with linearly polarized fraction 44(3)%. Linearly polarized radio sources exhibit Faraday rotation of the polarization angle on the sky by angle $\phi_{\text{far}} = \text{RM}\lambda^2$, where λ is the wavelength and the rotation measure, a measure of magnetization, is the line of sight component of the magnetic field weighted by the electron density:

$$\text{RM} = 0.812 \text{ rad m}^{-2} \int \frac{n_e}{\text{cm}^{-3}} \frac{B_{\parallel}}{\mu\text{G}} \frac{dl}{\text{pc}}.$$

We detect the expected λ^2 modulation pattern in the polarization as shown in Figure 2. The best-fit RM is $-186.1(1.4) \text{ rad m}^{-2}$. All radio telescopes have polarization leakage, an instrument-induced false polarization of unpolarized sources. We have mapped the leakage at GBT across the beam profile and throughout the passband and find leakage can produce false linear polarization as large as 10% and false circular polarization as large as 30%. Leakage-produced apparent polarization lacks the λ^2 wavelength dependence that we see in the linear polarization data and cannot produce the 44% polarization we detect so we conclude the linear polarization is of astronomical origin rather than due to leakage.

The detected rotation measure and dispersion measure imply an electron-weighted average line-of-sight component of the magnetic field of $0.38 \mu\text{G}$, compared to typical large-scale fields of $\sim 10 \mu\text{G}$ in spiral galaxies²⁷. This field strength is a lower limit for the magnetized region due to cancellations along the line of sight. Also, the magnetized region may only weakly overlap the dispersing region and so electron weighting may not be representative.

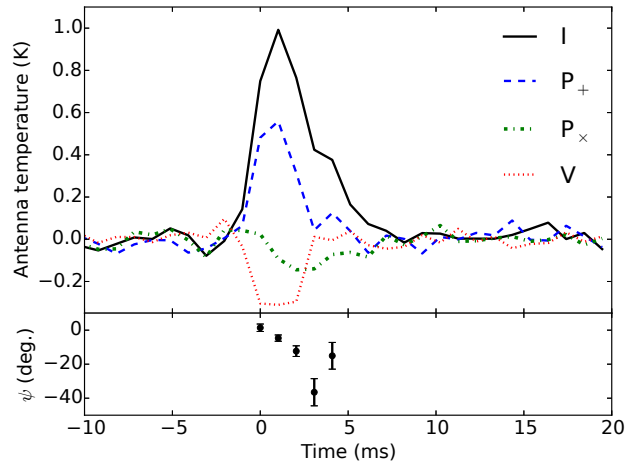


Figure 3: **Polarized pulse profiles averaged over spectral frequency.** Plotted is total intensity (I), linear polarization (P_+ and P_-), and circular polarization (V, may be instrumental). Before taking the noise-weighted mean over frequency, the data are scaled to 800 MHz using the best-fit spectral index and the linear polarization is rotated to compensate for the best-fit Faraday rotation. The linear polarization basis coordinates are aligned with (+), and rotated with respect to (\times), the mean polarization over time. Bottom panel shows the polarization angle (where measurable) in these coordinates. The error bars show the standard error based on simulations.

The magnetization we detect is likely local to the FRB source rather than in the Milky Way or the intergalactic medium (IGM). Models of Faraday rotation within the Milky Way predict a contribution of $\text{RM} = 18(13) \text{ rad m}^{-2}$ for this line of sight, while the IGM can contribute at most $|\text{RM}| = 6 \text{ rad m}^{-2}$ on a typical line of sight from this redshift²⁸.

We detect a rotation of the polarization angle over the pulse duration of $-0.25(5) \text{ radian ms}^{-1}$, shown in Figure 3. Such rotation of polarization is often seen in pulsars and is attributed to the changes in the projection of the magnetic field compared to the line of sight as the neutron star rotates²⁹.

We also detect circular polarization at roughly the 23% level, but that level of polarization might be due to instrumental leakage. Faraday rotation is undetectable for circular polarization, so the λ^2 modulation we use to identify astronomical linear polarization is not available as a tool to rule out leakage. For these reasons we do not have confidence that the detected circular polarization is of astronomical origin.

Radio emissions are often scattered: lensing by plasma inhomogeneities creates multiple propagation paths, with individual delays. We observe two distinct scattering time scales in the FRB 110523 data, indicating the presence of two scattering screens. In five previous FRB detections an exponential tail in the pulse profile was detected, interpreted as the superposition of delayed versions of the narrower intrinsic profile. The average scattering time constant for FRB 110523 is 1.66(14) ms at 800 MHz, with the expected decrease with spectral frequency as shown in Extended Data Figure 2. We also detect scintillation, the variation of intensity with frequency due to multi-path interference. We measure a scintillation decorrelation bandwidth $f_{\text{dc}} = 1.2(4) \text{ MHz}$ (see Extended Data Figure 3), indicating a second source of scattering with delays of order $1/f_{\text{dc}} \sim 1 \mu\text{s}$. This scintillation is consistent with Galactic expectations for this line of sight.

Scintillation should only occur if the first scattering screen is unresolved by the second, and we use this fact to constrain the bulk of the scattering material in the first screen to lie within 44 kpc of the source—roughly the scale of a galaxy (see Methods). It was previously unknown whether the $\sim \text{ms}$ scattering observed in FRBs was due to weakly scattering material broadly distributed along the line of sight or strong scattering near the source³⁰, but our detection of scintillation eliminates the distributed scat-

tering models. The observed scattering is too strong to be caused by the disks of host galaxies²³ and therefore the FRB source must be associated with either a strongly-scattering compact nebula or with the dense inner regions of its host galaxy. Either could produce the observed rotation measure, whereas most lines of sight through the ISM of a randomly oriented galactic disk contribute an order of magnitude less rotation measure²⁸.

Magnetization and scattering located near the FRB source disfavor models that involve collisions of compact objects such as white dwarfs or neutron stars¹⁴ since these older stellar populations are generally not associated with compact nebulae nor are they preferentially found near galactic centres. In contrast, a variety of models involving young stellar populations—including magnetar starquakes, delayed formation of black holes after core-collapse supernovae, and pulsar giant pulses^{16–18}—provide natural explanations for the properties we observe. Here scattering and magnetization occur in the surrounding young supernova remnants or star-forming regions, and the polarization properties we report are plausible given that these proposed emission mechanisms involve spinning magnetized compact objects. Precise model testing, beyond these general comments, will have to wait for more data which will determine if the magnetization and scattering features we report are generic.

1. Lorimer, D. R., Bailes, M., McLaughlin, M. A., Narkevic, D. J. & Crawford, F. A Bright Millisecond Radio Burst of Extragalactic Origin. *Science* **318**, 777–780 (2007).
2. Keane, E. F., Stappers, B. W., Kramer, M. & Lyne, A. G. On the origin of a highly dispersed coherent radio burst. *Monthly Notices of Royal Astronomical Society* **425**, L71–L75 (Sept. 2012).
3. Thornton, D. *et al.* A Population of Fast Radio Bursts at Cosmological Distances. *Science* **341**, 53–56 (July 2013).
4. Spitler, L. G. *et al.* Fast Radio Burst Discovered in the Arecibo Pulsar ALFA Survey. *Astrophysical Journal* **790**, 101 (Aug. 2014).
5. Burke-Spolaor, S. & Bannister, K. W. The Galactic Position Dependence of Fast Radio Bursts and the Discovery of FRB011025. *Astrophysical Journal* **792**, 19 (Sept. 2014).
6. Petroff, E. *et al.* A real-time fast radio burst: polarization detection and multiwavelength follow-up. *Monthly Notices of Royal Astronomical Society* **447**, 246–255 (Feb. 2015).
7. Ravi, V., Shannon, R. M. & Jameson, A. A Fast Radio Burst in the Direction of the Carina Dwarf Spheroidal Galaxy. *Astrophysical Journal Letters* **799**, L5 (Jan. 2015).
8. Champion, D. J. *et al.* Five new Fast Radio Bursts from the HTRU high latitude survey: first evidence for two-component bursts. *ArXiv e-prints*. arXiv:1511.07746 [astro-ph.HE] (Nov. 2015).
9. Rane, A. *et al.* A search for rotating radio transients and fast radio bursts in the Parkes high-latitude pulsar survey. *ArXiv e-prints*. arXiv:1505.00834 [astro-ph.HE] (May 2015).
10. Taylor, M. *et al.* The Core Collapse Supernova Rate from the SDSS-II Supernova Survey. *Astrophysical Journal* **792**, 135 (Sept. 2014).
11. Inoue, S. Probing the cosmic reionization history and local environment of gamma-ray bursts through radio dispersion. *Monthly Notices of Royal Astronomical Society* **348**, 999–1008 (Mar. 2004).
12. Ioka, K. The Cosmic Dispersion Measure from Gamma-Ray Burst Afterglows: Probing the Reionization History and the Burst Environment. *Astrophysical Journal Letters* **598**, L79–L82 (Dec. 2003).
13. Loeb, A., Shvartzvald, Y. & Maoz, D. Fast radio bursts may originate from nearby flaring stars. *Monthly Notices of Royal Astronomical Society* **439**, L46–L50 (Mar. 2014).
14. Kulkarni, S. R., Ofek, E. O., Neill, J. D., Zheng, Z. & Juric, M. Giant Sparks at Cosmological Distances? *Astrophysical Journal* **797**, 70 (Dec. 2014).
15. Geng, J. J. & Huang, Y. F. Fast Radio Bursts: Collisions between Neutron Stars and Asteroids/Comets. *Astrophysical Journal* **809**, 24 (Aug. 2015).
16. Lyubarsky, Y. A model for fast extragalactic radio bursts. *Monthly Notices of Royal Astronomical Society* **442**, L9–L13 (July 2014).
17. Falcke, H. & Rezzolla, L. Fast radio bursts: the last sign of supramassive neutron stars. *Astronomy & Astrophysics* **562**, A137 (Feb. 2014).
18. Connor, L., Sievers, J. & Pen, U.-L. Non-Cosmological FRB's from Young Supernova Remnant Pulsars. *ArXiv e-prints*. arXiv:1505.05535 [astro-ph.HE] (May 2015).
19. Chang, T.-C., Pen, U.-L., Bandura, K. & Peterson, J. B. An intensity map of hydrogen 21-cm emission at redshift $z \sim 0.8$. *Nature* **466**, 463–465 (July 2010).
20. Masui, K. W. *et al.* Measurement of 21 cm Brightness Fluctuations at $z \sim 0.8$ in Cross-correlation. *Astrophysical Journal Letters* **763**, L20 (Jan. 2013).
21. Switzer, E. R. *et al.* Determination of $z \sim 0.8$ neutral hydrogen fluctuations using the 21-cm intensity mapping autocorrelation. *Monthly Notices of Royal Astronomical Society* **434**, L46–L50 (July 2013).
22. Cordes, J. M. & Lazio, T. J. W. NE2001.I. A New Model for the Galactic Distribution of Free Electrons and its Fluctuations. *ArXiv Astrophysics e-prints*. eprint: astro-ph/0207156 (July 2002).
23. Katz, J. I. Inferences from the Distributions of Fast Radio Burst Pulse Widths, Dispersion Measures and Fluences. *ArXiv e-prints*. arXiv:1505.06220 [astro-ph.HE] (May 2015).
24. Tuntsov, A. V. Dense plasma dispersion of fast radio bursts. *Monthly Notices of Royal Astronomical Society* **441**, L26–L30 (June 2014).
25. Dennison, B. Fast radio bursts: constraints on the dispersing medium. *Monthly Notices of Royal Astronomical Society* **443**, L11–L14 (Sept. 2014).
26. Maoz, D. *et al.* Fast radio bursts: the observational case for a Galactic origin. *Monthly Notices of Royal Astronomical Society* **454**, 2183–2189 (Dec. 2015).
27. Widrow, L. M. Origin of galactic and extragalactic magnetic fields. *Reviews of Modern Physics* **74**, 775–823 (2002).
28. Oppermann, N. *et al.* Estimating extragalactic Faraday rotation. *Astronomy & Astrophysics* **575**, A118 (Mar. 2015).
29. Radhakrishnan, V. & Cooke, D. J. Magnetic Poles and the Polarization Structure of Pulsar Radiation. *Astrophysics Letters* **3**, 225 (1969).
30. Macquart, J.-P. & Koay, J. Y. Temporal Smearing of Transient Radio Sources by the Intergalactic Medium. *Astrophysical Journal* **776**, 125 (Oct. 2013).

Acknowledgements K. M. is supported by the CIFAR Global Scholars Program. T.-C. C. acknowledges support from MoST grant 103-2112-M-001-002-MY3. X. C. and Y.-C. L. are supported by MOST 863 program 2012AA121701, CAS XDB09000000 and NSFC 11373030. P. T. T. acknowledges support from NSF Award 1211781. J. B. P. acknowledges support from NSF Award 1211777. Computations were performed on the GPC supercomputer at the SciNet HPC Consortium.

Author Contributions K. M. integrated the FRB search routines into a software program; calibrated and filtered the raw FRB event data; performed scintillation analysis; led survey planning; produced Figure 2, Figure 3, and Extended Data Figure 3; and contributed to model fits to the FRB event, result interpretation, beam characterization, observations, data handling, and data validation. H.-H. L. performed the visual search of the search of over 6000 images, and discovering the FRB event. He also coproduced Figures 1 and Extended Data Figure 2, and contributed to the FRB search software program, observations, data handling, and data validation. J. S. wrote dedispersion and FRB search software routines; performed model fits to the FRB event including extracting the dispersion measure, rotation measure, scattering tail, and polarization angle swing; and contributed to result interpretation. C. J. A. contributed to observations, data handling, and data validation. T.-C. C. contributed to survey planning, observations, and data validation. X. C. contributed to data validation. A. G. contributed to FRB search algorithm validation. M. J. contributed to observations and data validation. C.-Y. K. contributed to observations and data validation. Y.-C. L. performed scintillation analysis on foreground pulsar and contributed to data validation. Y.-W. L. contributed to polarization leakage characterization, calibration methods, and data validation. M. M. contributed to result interpretation, analysis of the follow-up data, scintillation analysis on the foreground pulsar, and edited the manuscript. U.-L. P. carried out Faraday rotation measure synthesis resulting in detection of linear polarization and contributed to result interpretation, scintillation analysis, survey planning, and data validation. J. B. P. led manuscript preparation and contributed to result interpretation, survey planning, data validation. A. R. performed survey of archival multi-wavelength catalogues for coincident sources, coproduced Figures 1, produced Extended Data Figure 1, and added event simulation functionality to the FRB search software program. P. T. T. contributed to observations and data validation and editing the manuscript. T. V. led observational campaign and contributed to calibration methods, survey planning, data handling, and data validation. J. K. Y. contributed to data validation.

Competing Interests The authors declare that they have no competing financial interests.

Correspondence Correspondence and requests for materials should be addressed to K. M. (email: kiyo@physics.ubc.ca).

Methods

Data and pre-processing Our survey was conducted with the GBT linearly-polarized prime-focus 800 MHz receiver. For the digital back-end we used the GBT Ultimate Pulsar Processing Instrument. The data were collected with the telescope scanning 4 degrees/minute at constant altitude angle.

To act as a stable flux reference, a broadband noise source injects power at the feed point, producing a square wave of intensity with period locked at 64 times the 1.024 ms cadence. In the on-state the noise source increases the total power by approximately 10%. The switching noise source must be removed from the data before the search for transients can proceed. This is done by accumulating, over the one-minute scan, the periodic component with a period of 64 ms. The data are then normalized to the noise source amplitude in each spectral channel, providing an approximate bandpass calibration, and the noise source waveform is subtracted. For the search phase this level of calibration is sufficient and no absolute calibration is applied.

Analysis of the discovered event requires a more rigorous calibration than the search. We separately reference the vertical and horizontal polarization signals to the calibration noise source, with the noise source in turn referenced to a bright unpolarized point source (3C48) scanned 6.5 hours before the event, providing an on-sky calibration at each frequency and polarization. This results in an overall absolute flux calibration uncertainty of 9%²⁰. To calibrate the phase of the cross-correlation between the two antenna polarizations, which we need to measure polarization parameters Stokes U and V, we assume that the noise source injects the same signal into each with the same phase. Lab tests of the 800 MHz receiver verify this assumption except in the two spectral resonances of the receiver and in the edges of the band, which we discard. This procedure produces a one percent polarization calibration at the centre of the beam. The polarization characteristics off beam centre are described below.

The data contain several spectral channels that are irrecoverably contaminated by man-made radio frequency interference (RFI), largely due to cell phones. These are identified by anomalously high variance or skewness relative to other channels and all data from these channels are discarded. A total of 3836 out of 4096 channels (93.6%) pass the RFI cuts.

Prior to searching the data for FRBs, Galactic and extragalactic synchrotron continuum emission is removed. Such emission is broadband and varies on much longer time scales than FRB events and can thus be removed by a variety of algorithms. For the search, where computational efficiency is a concern, a continuum template is formed for each 38 second block of data by performing a mean over frequency. This template is then correlated against each spectral channel and the contribution subtracted.

When analysing the discovered event, computational complexity is less of a concern so we high-pass filter the data on 200 ms time scales. The filtering substantially reduces the variance of the data, and we perform another iteration of identification of RFI contaminated spectral channels.

Searching the data To search for FRBs we concentrate the energy of possible events into a few pixels of an image, using a dedispersion algorithm we developed. In the array of spectra shown in Figure 1, the event is spread out in both time and frequency. We need to remove this dispersion, aligning the arrival times across frequency, then average over frequency to produce a time series that has the pulse energy localized. Since we do not know the dispersion measure a priori we dedisperse over a range of trial values of DM from 0 to 2000 pc cm⁻³. The dedispersion process produces a set of frequency-averaged intensities versus time and DM. We use a modified tree dedispersion algorithm³¹. We developed a recursive program for this algorithm that, running on a single desktop computer, carries out the dedispersion in 10% of real time.

After transforming to DM-time space, we need to search each DM for bursts of unknown duration and unknown profile, which we accomplish using a set of boxcar integrals over time, of lengths ranging from 1 ms to the block length of 38 seconds. Blocks overlap by 8 seconds so events straddling blocks are not missed. The search algorithm also accumulates noise statistics at each DM for each boxcar length. The procedure is easily parallelized by distributing data files among nodes of a large computer

array. A software package used to search our data for transient events is publicly available³².

The above procedure produced 6496 DM-time plots, which we visually inspected. We find only one clear FRB candidate—FRB 110523—but the search also turned up the previously known pulsars J2139+00 and J0051+0423, roughly in line with expectations given survey parameters.

We have yet to perform a detailed analysis of the completeness of our search but taken at face value our single detection implies an all-sky rate of $\sim 5 \times 10^3$ per day above a fluence of threshold of ~ 1 Jy ms, assuming an effective sky coverage of 0.3 sq. deg., in-line with previous estimates.

To provide a set of training templates for the visual search, simulated rectangular pulses were added onto a sample of data which included no significant events. An example of a simulated event is shown in Extended Data Figure 1. The simulated event shows a characteristic ‘hourglass’ feature in the DM-time plots.

Modeling the pulse profile and polarization We use Markov-Chain Monte Carlo methods to fit a model to the FRB event and measure its properties. Throughout the analysis we assume the noise is Gaussian and treat it as uncorrelated between channels, with per-channel weights estimated from their variances. This simplification allows us to forgo the time-consuming process of Fisher matrix statistical analysis. The assumption is slightly incorrect: the data are χ^2 distributed with 50 degrees of freedom. We also find that adjacent frequency channels are actually 2.5% correlated by the Fourier transform filter used for spectral channelization. No significant correlation is detected between more widely separated channels. We account for adjacent channel correlation by increasing all errors by 2.5%.

To create a model intensity profile for comparison to the data we begin with a Gaussian pulse profile in time, with width σ which is independent of frequency. This is convolved with a one-sided exponential scattering kernel with a frequency-dependent duration to yield the normalized pulse profile:

$$f(\nu, t) = \left[\frac{1}{\sqrt{2\pi}\sigma^2} \exp\left(-\frac{t^2}{2\sigma^2}\right) \right] \otimes \left[\theta(t) \frac{1}{\tau_\nu} \exp\left(-\frac{t}{\tau_\nu}\right) \right], \quad (1)$$

where $\theta(t)$ is the Heaviside step function, $\tau_\nu = \tau(\nu/\nu_{\text{ref}})^{-4}$, the frequency dependence expected for scattering, and τ is the scattering time at ν_{ref} . In the final spectrum we allow for spectral index α of the overall intensity and delay the pulse for dispersion:

$$I(\nu, t) = A \left(\frac{\nu}{\nu_{\text{ref}}} \right)^\alpha f(\nu, t - t_\nu) \quad (2)$$

where A is the burst amplitude at reference frequency ν_{ref} , $t_\nu = t_0 + \text{DM} \times \text{DM}_0 (\nu^{-2} - \nu_{\text{ref}}^{-2})$, $\text{DM}_0 = 4148.808 \text{ MHz}^2 \text{ pc}^{-1} \text{ cm}^3 \text{ s}$, DM is the dispersion measure of the burst, and t_0 is the burst arrival time at ν_{ref} . While in principle the choice of the reference frequency ν_{ref} is arbitrary, in practice we find a value of 764.2 MHz, near the centre of the signal-to-noise weighted band, substantially decorrelates the fit parameters. This constitutes our base unpolarized model. Circular polarization is modelled in the same way as total intensity.

Our base linearly polarized model is the same as the unpolarized model with an added Faraday rotation factor:

$$[Q + iU](\nu, t) = I \exp[2i\text{RM}(\lambda^2 - \lambda_{\text{ref}}^2) + i\phi_0], \quad (3)$$

where RM is the rotation measure, ϕ_0 is the polarization angle at the reference frequency and pulse centre, and I is the model for intensity given above. We find the likelihood surfaces are quite close to Gaussian, and so the Markov chains converge quickly. We run an initial short chain to estimate the covariance matrix, then run 4 chains of length 500,000 steps to estimate parameters. This approach gives good convergence (the Gelman-Rubin convergence $r - 1$ is typically 0.005).

To search for time dependence of the polarization angle, we extend the model to allow the polarization angle to vary linearly with time. We did this fit two ways: 1) apply the phase gradient to the pre-scattering Gaussian burst and then convolve with the scattering kernel, and 2) apply the

gradient to the scattering-convolved burst profile. While the first is more physically natural if the rotation happens at the burst source before scattering, we find that the second (post-scattering gradient) provides a significantly better fit (5.4σ significance *c.f.* 2.1σ) and quote results for this fit. We attribute this to substructure in the polarized pulse, that is poorly modelled by a Gaussian with linearly changing polarization angle. We do not have enough signal to noise to further investigate the substructure but the conclusion that the polarization angle rotates is robust.

The plasma delay as a function of frequency is expected to follow a ν^{-2} power law, scattering time should have frequency dependence near ν^{-4} , and the Faraday rotation angle should be proportional to ν^{-2} . We extend the model used in the Markov chains to test these predictions, fitting for the dispersion measure index, scattering index, and rotation measure index. All fit parameters are listed in Extended Data Table 1 with results grouped by independent fits.

To check our analysis software and calibration (especially the polarization sign) we performed observations of pulsar B2319+60. The pulsar data were processed using the FRB pipeline and the Faraday rotation measured from a single pulse. The rotation measure was determined to be $-239.9(4) \text{ rad m}^{-2}$, in good agreement with the published value³³, and under this sign convention the FRB's RM is negative.

GBT beam During the two second period over which the FRB pulse traverses the bandpass, the pointing centre of the GBT beam scans 8 arcminutes, which is about half the FWHM beam width. The pulse intensity increases steeply during the arrival period likely indicating that the source coordinates moved from the edge of the GBT beam at the start of the arrival period to a position closer to the beam centre as lower frequencies arrived. The GBT beam is also wider at lower frequencies which also contributes to the steep spectral index. Simulations indicate that this picture is consistent although, due to the unknown intrinsic spectral index of the source and unknown impact parameter of the scan relative to the source, we are unable to use this information to obtain a precise localization.

It is highly unlikely that the burst entered the telescope through a sidelobe. Because of its off-axis design, GBT has low sensitivity in its sidelobes. Simulated models of the 800 MHz receiver beam show the first sidelobe to be a ring around the primary beam with radius 0.6 deg., width 0.1 deg., and 30 dB less sensitivity than boresight (Sivasankaran Srikanth, personal communication, November 2012). The second and third sidelobes have similar geometry, occurring 0.8 and 1.0 deg. from boresight and suppressed by 37 and 40 dB respectively. These near sidelobes do not cover significantly more sky area than the main beam and with their dramatically lower sensitivity it is unlikely that the lobe would contribute to the burst detection rate.

Subsequent sidelobes have even less sensitivity but cover more area. They are ruled out by the observed spectrum of FRB 110523. The radial width of the sidelobes is 0.1 deg. and their radial locations are inversely proportional to observing frequency. As such, if the burst had entered a far sidelobe we would have observed far more spectral structure; several peaks and nulls. Even the previously discussed first sidelobe is in tension with the observed spectrum when accounting for the added spectral structure expected from ~ 0.1 deg. of scanning during the pulse arrival period. For the first three sidelobes it is possible that, though an improbable coincidence, the telescope's scanning could cancel the location spectral dependence of the sidelobes. However as previously argued, a source location in the sidelobes is unlikely due to their combination of low sensitivity and low area.

To determine the polarization properties of the primary beam, we have performed on-axis and off-axis measurements of the beam using both bright point sources and pulsars. Such measurements are crucial for our survey's primary science goal of mapping cosmic structure through the 21 cm line. We find that while GBT's off-axis design reduces sidelobe amplitude it leads to substantial polarization leakage in the primary beam. On boresight, the leakage from total intensity to polarization is less than one percent. Off boresight, leakage peaks at approximately 0.2 deg. in the azimuth direction. Leakage from Stokes I to Q/U is several percent of the forward gain and from Stokes I to V it is as high as 10%. When comparing

to the gain at that location in the beam instead of the forward gain, these numbers translate to 10% leakage to linear polarization and 30% leakage to circular. The leakage is only weakly dependent on frequency. These measurements are in agreement with simulated beam models.

The observed polarization angle rotation over the duration of the pulse cannot be due to leakage. The rotation occurs in each frequency bin over a few milliseconds, during which time the GBT beam centre moves just 7 milliarcseconds. Gradients of the leakage pattern at such small difference of angle are much too small to explain the change of polarization angle. To achieve the signal to noise sufficient to detect the angle swing it is necessary to integrate over frequency, introducing the two-second timescale associated with dispersion delay, but the integrand is composed of millisecond differences of polarization angle, making the two-second timescale irrelevant.

Scintillation Since we only see the FRB pulse for a few milliseconds we have no information on variation of the flux on longer time scales, and concentrate on quantifying the scintillation-induced variation of intensity with frequency by calculating the de-correlation bandwidth. We first form $\delta T(\nu) \equiv T(\nu)/T_{\text{smooth}}(\nu)$ where $T_{\text{smooth}}(\nu)$ is the power law fit to the spectrum, accounting for the intrinsic spectrum of the event as well as the frequency dependence and motion of the telescope beam. We then form the correlation function

$$\xi(\Delta\nu) \equiv \langle \delta T(\nu) \delta T(\nu + \Delta\nu) \rangle_\nu. \quad (4)$$

This correlation function is estimated from the observed spectrum and is shown in Extended Data Figure 3.

To estimate the de-correlation bandwidth, f_{dc} , from the observed correlation function, we fit to the Fourier transform of an exponential scattering function³⁴:

$$\xi_{\text{model}}(\Delta\nu) = \frac{m}{f_{\text{dc}}^2 + \Delta\nu^2}. \quad (5)$$

This fit yields $f_{\text{dc}} = 1.2(4) \text{ MHz}$ and $m = 0.26(8)$. The errors on the measurement of the correlation function depend on the underlying statistics of the scintillation, which are both non-Gaussian and model-dependent³⁵. We estimate the errors in Extended Data Figure 3 through simulations, with errors on fit parameters subsequently expanded to account for modelling uncertainties.

Two-screen model for scintillation and scattering The observed scintillation de-correlation bandwidth is comparable to that observed for Galactic pulsar J2139+00, less than two degrees away from FRB 110523 on the sky and at a distance of 3 kpc based on its dispersion measure³⁶, indicating the scintillation arises from the Galactic interstellar medium.

A familiar form of scintillation in optical astronomy is the twinkling of stars. Optical scintillation is due to turbulence in the atmosphere and is commonly modelled by projecting the optical medium onto a screen above the telescope with micro-images appearing in the plane of this screen. For stars, rapid variation of flux with frequency are seen because stars have angular size small enough that light emitted from opposite edges of the stellar disk has path length difference less than a wavelength. Stars are said to be unresolved by the scintillation screen, meaning that they are indistinguishable from point sources. The multipath interference changes with time because of turbulent motions in the atmosphere. Planets, in contrast to stars, have angular size resolved by the screen, so the flux variations are typically a small fraction of the total flux. For similar reasons, among radio sources, pulsars often show scintillation, while the much larger extragalactic radio sources do not. At radio wavelengths scattering occurs in the intervening plasma rather than the atmosphere.

To model scintillation and scattering for FRB 110523 we project the intervening material onto two screens, representing the material in the Milky Way and in the host galaxy, respectively. We use two screens because the scintillation and scattering have very different time scales, which precludes modelling with a single screen. As with optical scintillation each screen produces a halo of micro-images, which can be considered scattering sites. Propagation via a micro-image at the edge of a halo requires a longer propagation time from source to observer than micro-images near the centre. In our model the delays associated with the Galactic screen produce the

micro-second scintillation path differences, while the host screen path differences produce the 1.6 ms exponential tail of the pulse profile.

In our two-screen model the presence of strong scintillation indicates that the host screen is unresolved by the Galactic screen, and this allows an estimate of the host screen position. We assume the position of the Galactic screen is the characteristic thickness of the ionized Galactic plane $D=1$ kpc. The angular size the Galactic screen is then given by $\theta = \sqrt{2c\tau}/D \sim 1$ mas and the resolving power of the Galactic screen is $\rho = \lambda/(\theta D) \sim 600$ nas. The scintillation would be washed out if the host screen exceeded this angular size. This small angular size combined with the 1.6 ms scattering time places the host scattering screen within 44 kpc of the source, assuming the maximum source distance of ~ 1 Gpc (constrained by the observed dispersion measure).

To further test our scintillation and scattering model, we compared the scintillation of the main pulse to the scintillation in the scattering tail by cross-correlating the intensity spectrum early in the pulse to the spectrum late in the pulse. To obtain the early pulse spectrum, we use a filter matched to the Gaussian part of the profile with no scattering tail. For the late part we use a filter matched to the tail beginning 3 ms into the pulse. The cross de-correlation bandwidth is $f_{dc} = 1.3(5)$ compared to $f_{dc} = 1.1(6)$ MHz and $f_{dc} = 1.0(4)$ MHz for the early and late pulse respectively. Correlation amplitudes are $m = 0.30(9)$, $m = 0.18(8)$, and $m = 0.47(13)$ for the cross correlation, early, and late pulse respectively. These are all consistent with the level of scintillation measured for the full pulse, indicating that the most direct path and scattering-delayed micro-images share a common scintillation-induced spectrum. The scintillation source is therefore separate from the source of the scattering tail, and we place them in the Milky Way and host galaxy respectively.

Follow-up observations We carried out observations at the position of FRB 110523 from 700 MHz to 900 MHz at three separate epochs on MJDs 57134, 57135, and 57157 for durations of 1.8 hrs, 1.8 hrs, and 3 hrs, respectively. We detected no bursts with DMs in the range of 0 to 5000 pc cm⁻³ with significance greater than 6 sigma. We also performed a periodicity search on the data, and detected no pulsar candidates. The estimated limiting flux density of this search, assuming a pulsar duty cycle of 10%, was 0.04 mJy.

Counterpart sources To identify possible optical counterpart source candidates we searched the Sloan Digital Sky Survey (DR12) catalogues³⁷ throughout a region centred on the position of the radio beam at the time the pulse arrived at 700 MHz. The beam size of the GBT is 15 arcminutes FWHM, but we expanded the search area to 30 arcminutes diameter to account for a source lying outside the FWHM beam area. Within this field there are 70 objects identified as galaxies in the catalogue of which 40 are listed as having redshift less than 0.5. The 100% galactic completeness limit of SDSS photometry³⁸ is r-band magnitude 21. As such, all Milky Way-like galaxies are included for $z < 0.28$, assuming an absolute magnitude $M_r \approx -19.86$.

No X-ray or gamma-ray sources are listed in the NASA/IPAC Extragalactic Database in this region.

Data availability The raw data used in this publication are available at <http://www.cita.utoronto.ca/~kiyo/release/FRB110523>.

Code availability The code used to search the data archive for FRB events is available at https://github.com/kiyo-masui/burst_search.

The code used to analyse the discovered FRB is available at https://github.com/kiyo-masui/FRB110523_analysis.

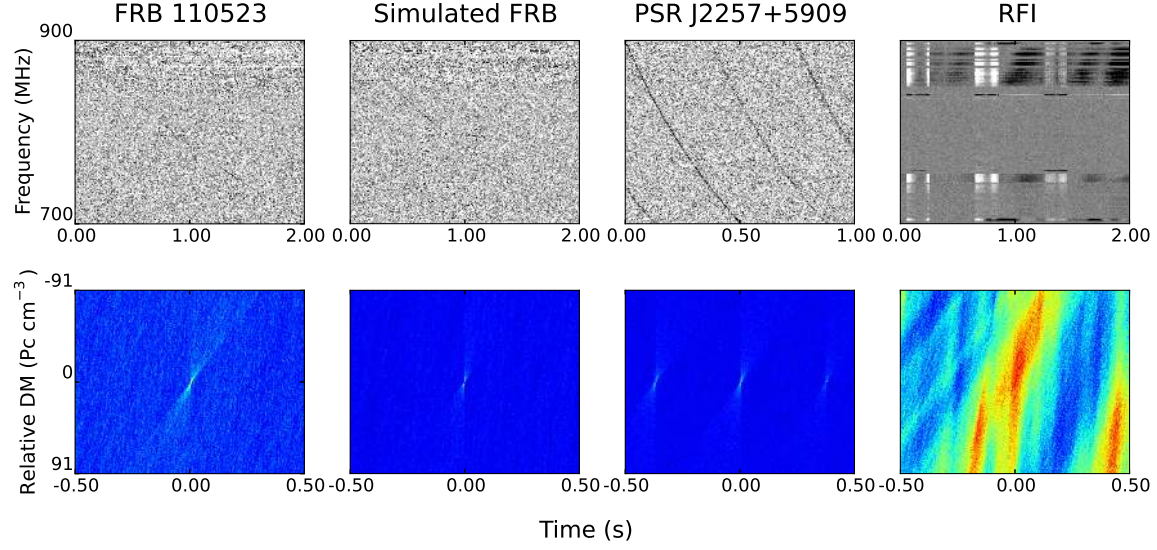
35. Johnson, M. D. & Gwinn, C. R. Ultra-high-resolution Intensity Statistics of a Scintillating Source. *Astrophysical Journal* **755**, 179 (Aug. 2012).
36. Taylor, J. H. & Cordes, J. M. Pulsar distances and the galactic distribution of free electrons. *Astrophysical Journal* **411**, 674–684 (July 1993).
37. Alam, S. *et al.* The Eleventh and Twelfth Data Releases of the Sloan Digital Sky Survey: Final Data from SDSS-III. *Astrophysical Journal Supplement* **219**, 12 (July 2015).
38. Yasuda, N. *et al.* Galaxy Number Counts from the Sloan Digital Sky Survey Commissioning Data. *Astronomical Journal* **122**, 1104–1124 (Sept. 2001).

31. Taylor, J. H. A Sensitive Method for Detecting Dispersed Radio Emission. *Astronomy and Astrophysics Supplement* **15**, 367 (June 1974).
32. https://github.com/kiyo-masui/burst_search.
33. Hamilton, P. A. & Lyne, A. G. Faraday rotation measurements on 163 pulsars. *Monthly Notices of Royal Astronomical Society* **224**, 1073–1081 (Feb. 1987).
34. Lorimer, D. R. & Kramer, M. *Handbook of Pulsar Astronomy* (Cambridge University Press, Dec. 2004).

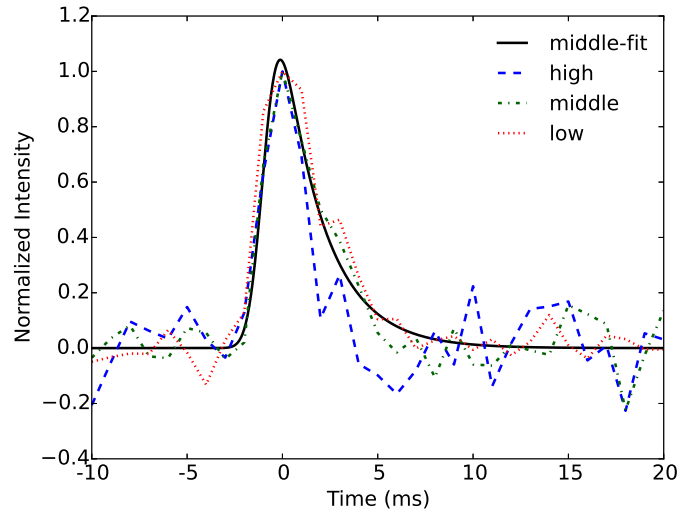
Extended Data

Barycentric $\nu = \infty$ arrival (MJD)	55704.62939511
GBT boresight at 900 MHz arrival	RA = 21 ^h 45 ^m 31 ^s Dec = −00 ^d 15 ^m 23 ^s $l = 56.0795^\circ$ $b = -37.9435^\circ$
GBT boresight at 700 MHz arrival	RA = 21 ^h 45 ^m 12 ^s Dec = −00 ^d 09 ^m 37 ^s $l = 56.1215^\circ$ $b = -37.8234^\circ$
Dispersion measure (pc cm ^{−3})	623.30(6)
Fluence at 800 MHz (K ms)	3.79(15)
Spectral index	−7.8(4)
Unscattered pulse FWHM (ms)	1.73(17)
Scattering time at 800 MHz (ms)	1.66(14)
Linear polarization fraction (%)	44(3)
Rotation measure (rad m ^{−2})	−186.1(1.4)
Polarization rotation rate (rad ms ^{−1})	−0.25(5)
Dispersion measure index	−1.998(3)
Scattering index	−3.6(1.4)
Faraday rotation index	−1.7(2)

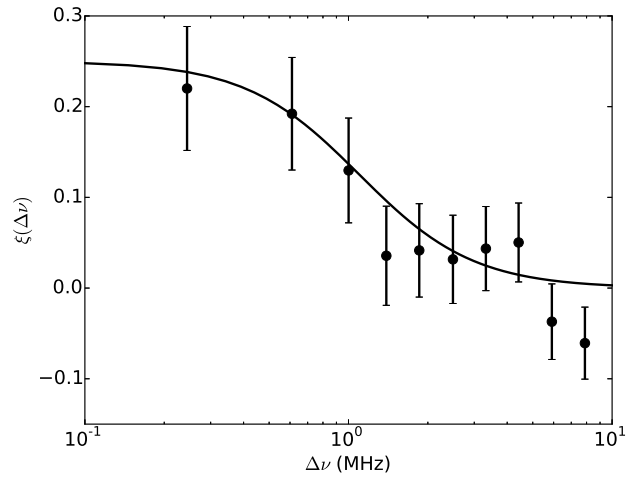
Extended Data Table 1: **FRB 110523 parameters**. Arrival time and astrometric parameters as well as parameters for fits of the base unpolarized, base polarized, and extended models to antenna temperature data. The steep spectral index we observe is attributed to beam effects. Statistical uncertainties enclose the 68% confidence interval of the measurement.



Extended Data Figure 1: **Events in Frequency-time and Dispersion Measure-time space.** From left to right: Data for FRB 110523; a simulated FRB; a known pulsar PSR J2257+5909; man-made Radio Frequency Interference. Brightness temperature is shown in frequency-time space (upper panels) and the same data in dispersion measure-time space (lower panels). Relative dispersion measure is the difference between the DM and the event DM; event DMs are 622.8, 610.3, 151.0, and 1132.1 pc cm^{-3} , respectively from left to right. The time axes of the frequency-time plots show time relative to the DM-t zero time. The colour scale in the lower panels represents broadband flux with red showing a bright source.



Extended Data Figure 2: **Pulse profiles for FRB 110523 in three sub-bands.** Each sub-band has width 66 MHz. The pulse width decreases with frequency (at 2.6-sigma significance), consistent with models of scattering in the interstellar medium. Also shown in black is the best-fit model profile for the middle band.



Extended Data Figure 3: **Spectral brightness correlation function of FRB 110523.** The intensity spectrum has structure that is correlated for frequency separations less than $f_{\text{dc}} = 1.2$ MHz. Error bars are standard errors estimated from simulations and are correlated.